JOURNAL OF SYNCHROTRON RADIATION

ISSN 1600-5775

Received 11 June 2018
Accepted 2 October 2018

Edited by V. Favre-Nicolin, CEA and Université Joseph Fourier, France

Keywords: synchrotron; X-ray diffraction; Fischer–Tropsch; catalysis.

Supporting information: this article has supporting information at journals.iucr.org/s

In situ observation of phase changes of a silica-supported cobalt catalyst for the Fischer–Tropsch process by the development of a synchrotron-compatible *in situ*/*operando* powder X-ray diffraction cell

Adam S. Hoffman,[a] Joseph A. Singh,[b,c,d] Stacey F. Bent[b,c] and Simon R. Bare[a,c]*

[a]Stanford Synchrotron Radiation Lightsource, SLAC National Accelerator Laboratory, Menlo Park, CA 94025, USA, [b]Department of Chemical Engineering, Stanford University, Stanford, CA 94305, USA, [c]SUNCAT Center for Interface Science and Catalysis, SLAC National Accelerator Laboratory, Menlo Park, CA 94025, USA, and [d]Department of Chemistry, Stanford University, Stanford, CA 94305, USA. *Correspondence e-mail: simon.bare@slac.stanford.edu

In situ characterization of catalysts gives direct insight into the working state of the material. Here, the design and performance characteristics of a universal *in situ* synchrotron-compatible X-ray diffraction cell capable of operation at high temperature and high pressure, 1373 K, and 35 bar, respectively, are reported. Its performance is demonstrated by characterizing a cobalt-based catalyst used in a prototypical high-pressure catalytic reaction, the Fischer–Tropsch synthesis, using X-ray diffraction. Cobalt nanoparticles supported on silica were studied *in situ* during Fischer–Tropsch catalysis using syngas, H_2 and CO, at 723 K and 20 bar. Post reaction, the Co nanoparticles were carburized at elevated pressure, demonstrating an increased rate of carburization compared with atmospheric studies.

1. Introduction

In situ observation of a catalyst under relevant working conditions (exposed to reactants at reaction temperature and/or pressure) is key in determining what active site, surface, structure or phase of the catalytic material is present and is responsible for the catalyst's activity or selectivity. Such information allows for the development of structure/activity relationships that give a fundamental understanding of catalysis science and drive the development of new catalytic materials. *In situ* measurements offer the advantage of studying the active state of a catalyst compared with conventional static or *ex situ* characterization that only captures the catalyst in a stable state (often in air) before or after the reaction, which may not be the same state of the material under working conditions. *In situ* characterization also allows for direct observation of transient states/species as reaction conditions are changed that are not observable in *ex situ* measurements. When coupled with analysis of the effluent gas stream, *operando* measurements yield the structure/activity relationships in one experiment without the need to correlate data between different experimental setups.

X-ray diffraction (XRD) is a commonly used technique to provide relevant information concerning crystalline materials, giving insight into the crystalline phases present, their average crystallite diameter *via* the Scherer equation, and information on the strain of the lattice and other more advanced properties. XRD can be applied to characterize bulk catalytic materials such as metal oxides, zeolites and metal organic

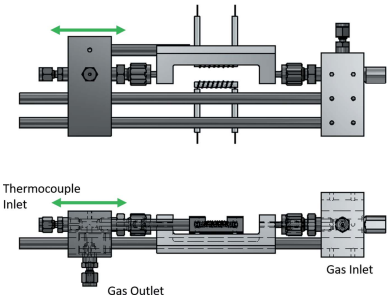

frameworks but can also be applied to the class of supported-metal catalysts, which consists of a small fraction of a catalytically active material, most commonly a precious metal, anchored to an inert support. XRD characterization of the supported metal catalyst not only determines the crystal structure of the support (*e.g.* silica, alumina, zeolite, ceria, zirconia) but is used to determine the average size and phase of the supported metal nanoparticles, assuming the particle is large enough for diffraction (typically >3 nm).

The need for XRD characterization of catalytic materials, together with the importance of *in situ* studies, has led to the development of several synchrotron-based *in situ* powder XRD cells for characterizing catalytic samples in non-air (inert or reactive) atmospheres at elevated temperatures and pressures (Chupas *et al.*, 2001, 2008; Clausen *et al.*, 1991; Jensen *et al.*, 2010; Tsakoumis *et al.*, 2012). The choice to perform the *in situ* XRD measurements at a synchrotron is advantageous due to: (i) higher angular resolution due to the high source collimation compared with conventional laboratory sources allowing for more accurate Rietveld refinement of powder samples; (ii) monochromatic X-rays, so no extra diffraction peaks exist from satellite lines; (iii) the availability of X-rays with higher energies that can penetrate through reactor walls; (iv) higher photon flux improving the signal-to-noise ratio, allowing for lower detection level and/or smaller sample size, and increasing data acquisition speeds so that *in situ* kinetics can be determined, and (v) the ability to combine the XRD method with other X-ray (Clausen *et al.*, 1993) or spectroscopic techniques (O'Brien *et al.*, 2009) for multi-modal sample characterization.

Herein we report the design, fabrication and testing of a powder XRD cell that operates at high temperatures (up to 1373 K) and pressures (35 bar) under gas flow for the *in situ* characterization of catalysts, and is fully compatible with the scattering beamlines at the Stanford Synchrotron Radiation Lightsource (SSRL). This XRD cell is an improvement on prior designs (Chupas *et al.*, 2008; Tsakoumis *et al.*, 2012) with the major advantages of reducing the failure rate of capillary installation and making it more versatile for use at multiple-scattering beamlines at SSRL. The XRD cell was tested through the *in situ* characterization of silica-supported cobalt nanoparticles under reduction, reaction and carburization conditions, described below, highlighting the cell's ability to perform through a range of temperatures and pressures. The silica-supported Co-based catalyst, Co/SiO_2, was selected as a test case because: (i) the material is of key importance as an industrial Fischer–Tropsch (F–T) catalyst (Ail & Dasappa, 2016; Khodakov *et al.*, 2007) and the F–T process involves conditions at elevated temperatures (473–673 K) and pressures (20–100 bar); (ii) the Co particles are large enough for study through XRD; and (iii) the Co particles have been shown to transform from $Co^{3+/4+}$ to Co^0 to Co_2C through the reduction, reaction and carburization steps (Cats & Weckhuysen, 2016; Karaca *et al.*, 2011; Singh *et al.*, 2018). *In situ* XRD has been used to study F–T catalysts but equipment limitations have limited experiments to 1–2 bar pressure (Staniuk *et al.*, 2014; Su *et al.*, 2016; de Smit *et al.*, 2009; Cats & Weckhuysen, 2016; Lebarbier *et al.*, 2011; Price *et al.*, 2017; Cats *et al.*, 2016), while some groups have designed equipment to characterize the catalysts at more industrially relevant pressure, 10–20 bar (Tsakoumis *et al.*, 2010, 2013; Cats *et al.*, 2013; Cats & Weckhuysen, 2016; Rønning *et al.*, 2010). As noted above, the design reported herein along with its predecessors (Chupas *et al.*, 2008; Tsakoumis *et al.*, 2012) will advance the F–T catalysis field as well as other catalytic or materials processes requiring more extreme temperature and pressure process conditions.

The specific treatment and reaction steps that were used to demonstrate the cell's performance were the following. (i) Reduction at 723 K of the Co/SiO_2 in a flow of hydrogen. This demonstrated the cell's capabilities to operate at high temperatures and ambient pressure. The results of the experiment showed that in the as-prepared calcined catalysts the cobalt started as Co_3O_4 nanoparticles (NPs) and went through a multistep reduction process during activation in H_2 to form metallic, face-centred cubic (f.c.c.), Co NPs. (ii) Reaction of the *in situ* reduced Co NPs with syngas (2:1 H_2:CO) at 20 bar and 523 K to observe the catalyst under reaction conditions. This test demonstrated the cell's performance at elevated pressure and temperature. The XRD data show that the metallic Co particles remain stable under the reaction conditions. (iii) Post-reaction, the hydrogen was removed from the feed stream leading to *in situ* carburization of the Co/SiO_2 catalyst. The at-pressure process showed an increased rate of carburization due to the elevated pressure compared with prior atmospheric carburization experiments (Karaca *et al.*, 2011). The improved time resolution, due to the use of a synchrotron source combined with the use of an area detector, demonstrated the utility of our configuration in resolving intermediate states that other studies (Cats & Weckhuysen, 2016) were unable to clearly resolve using XRD.

2. Current synchrotron powder XRD cells

There has been a near standardization in the design of synchrotron-compatible *in situ* powder XRD cells for the characterization of heterogeneous catalysts. A review of the literature shows that all cells use a thin-walled capillary to hold the powdered sample. Capillaries are readily available and are produced in a wide variety of materials, diameters and wall thicknesses, as previously discussed (Chupas *et al.*, 2008) and summarized in Table S1 of the supporting information. These capillaries allow for a range of operating temperatures and pressures with current maxima of 1430 K (this work) and 100 bar (Bansode *et al.*, 2014), respectively. Capillary selection is strongly dependent on the desired overall process conditions including the operating temperature and pressure, and the gas/liquid that the catalyst will need to be exposed to. Despite a common method of containing the catalyst, there are significant differences in the current designs centered on: (i) how the capillary is heated and/or its temperature is controlled; (ii) how the entire XRD cell is mounted at the beamline; and (iii) how the capillary is mounted into the cell.

These variations often make the designs synchrotron- and/or beamline-specific.

2.1. Heating the capillary

There are primarily two methods for heating *in situ* capillary powder XRD cells: forced hot air and radiative heating *via* resistive coils. Forced hot air heating has been implemented at HASYLAB, the Swiss Norwegian Beamline at ESRF, and Super XAS at the Swiss Light Source (Clausen *et al.*, 1991; Tsakoumis *et al.*, 2012). Supplying hot air from below the sample gives a large unobstructed area around the sample allowing for a large q-range to be collected and/or the addition of other optical probes for simultaneous multi-modal characterization making this design ubiquitous (de Smit *et al.*, 2010). However, there is some concern regarding thermal uniformity of the catalyst bed, especially if the capillary is larger than 2–3 mm in diameter and the catalyst bed length exceeds ~10 mm, due to the limited size of air stream from the heater. This method has improved safety compared with the resistive coils, discussed below, as the forced air prevents any potentially flammable chemicals from coming in contact with the heating elements.

Disadvantages of the forced hot air heating include the chosen method of temperature measurement and control, the additional infrastructure needed to operate the heater, and the overall high cost of the system. Current forced hot air designs control the temperature of the air at the outlet of the hot air gun, not at the actual sample position, requiring calibration and a known offset. This approach does remove the need to install a thermocouple in the capillary but additional corrections in the temperature measurement need to be made, and there is always some degree of uncertainty. An elegant solution to the lack of a thermocouple at the sample position is the addition of BN to the sample and the use of the known thermal expansion parameter of the BN lattice to determine the temperature at a given scan (Tsakoumis *et al.*, 2012). The necessary infrastructure makes this design large and 'beamline-specific' as the forced air heaters often require a 208 V AC supply, compressed house air, and cooling water to operate and thus the whole system is not readily portable from one beamline to the next.

Radiative heating *via* resistive coils has been implemented in a 'bottom only' design at ESRF (Jensen *et al.*, 2010) similar to the forced hot air heaters, and with an alternative design having twin coils mounted both above and below the capillary (Chupas *et al.*, 2001, 2008). Unlike the forced air heater, the temperature of the sample for the resistive heater designs is measured with a thermocouple inserted into the catalyst bed, ensuring more accurate temperature control and a true catalyst bed temperature. Both methods of heating have been tested to determine thermal uniformity (Broemme, 1991; Meunier, 2010) and the heated zones, often 10 mm in length, exhibit nearly uniform temperature, within a few K, but there is concern that larger-diameter capillaries may introduce a radial thermal heterogeneity. Since the resistive coils are custom made, they can be wound longer, shorter or on a larger-diameter support giving a larger degree of flexibility with respect to the length of the catalyst bed and diameter of the capillary. The addition of a second, top-mounted, heating element and the fact that the elements are placed in close, <1 mm, proximity to the capillary, does result in a more limited q-range for data collection and limits placement of additional spectroscopic probes for simultaneous multi-modal characterization. However, the only infrastructure needed is power, in the form of a DC power supply, resulting in a compact, portable design that can be installed on many different beamlines, and the overall cost is substantially less than the hot air design, USD 7000 *versus* USD 45000, respectively.

2.2. Mounting of the XRD cell at the synchrotron beamline

The mounting of *in situ* powder XRD cells at beamline endstations is dependent on the method of heating the sample. Cells that use forced hot air (Clausen *et al.*, 1991; Tsakoumis *et al.*, 2012) have sample cells that are mounted on a three-axis linear translation stage for positioning. Cells that rely on resistive heaters (Chupas *et al.*, 2001, 2008; Jensen *et al.*, 2010) are mounted on the goniometer of the diffractometer for positioning. The largest factor that determines the mounting scheme used for the two designs is the overall weight of the cell as the goniometer heads have a limited mass they can support with the resistive heaters being under the mass limit, and the forced air heaters being over it.

2.3. Mounting capillaries into the *in situ* powder XRD cells

The earlier *in situ* powder XRD cells relied on a compression fitting (*e.g.* Swagelok®) and a soft ferrule, often of polyimide (*e.g.* Vespel™) or graphite, to create a seal between the inlet/outlet fittings and the capillary (Chupas *et al.*, 2001, 2008; Clausen *et al.*, 1991; Jensen *et al.*, 2010). As there is a large error in the diameter of the capillary, *e.g.* a 3 mm borosilicate capillary typically has inlet and outlet dimensions of 4 mm and 2.5 mm, respectively, due to the fabrication technique, this either requires having a variety of ferrule dimensions available, or blank ferrules that have to be drilled to the correct dimension to allow sealing to the capillary dimensions. Additionally, using a compression seal presents additional challenges with the thinnest walled capillaries, 0.01 mm, as the compressive force can shatter the capillary during installation. Finally, if the XRD cell is not rigid enough, the mounting of the capillary into the cell can result in additional breakage if the cell flexes during installation or due to movement of the positioning stage.

There has been a report of a cell design where the capillary is epoxied into a U-shaped frame (Tsakoumis *et al.*, 2012), with the frame then being mounted in the XRD cell. This overcomes some of the disadvantages of directly mounting the capillary into the cell. Having a uniform opening to glue capillaries standardizes the compression fitting and removes the need for a variety of ferrules. This also removes the sealing challenges associated with variations in diameter as a function of length and batch that we have observed in drawn-style

glass/quartz capillaries. Finally, all the strain from tightening the ferrule or from bumps during movement of the cell is placed on the rigid support and not on the capillary, reducing the failure rate due to breakage. Disadvantages of the glued capillary include a limitation of the outer diameter of the capillary based upon the dimension of the mounting holes on the U-shaped frame, and the upper working temperature of the epoxy. However, such a design (Tsakoumis *et al.*, 2012) has been demonstrated to allow successful heating to a sample temperature of 673 K without affecting the seal created by the epoxy.

The published designs also have a fixed inlet and a movable outlet that slides on rods or rails that are adjusted to the length of the capillary during sample installation. This steel-on-steel linear motion may result in galling between the two surfaces, leading to sudden harsh movements of the cell and the attached capillary. This likely results in a high failure rate of the capillary during installation. However, combining these two designs, a compact resistive heated frame and a U-shaped frame for capillary support, improves the potential failure rate during installation while requiring fewer capillary-specific parts. The potential of galling still exists on the rods of such designs during capillary installation, offering possibilities for additional improvement.

3. Current design

Our design, shown in Fig. 1 with full schematics available in the supporting information, combines the advantages of the resistive heater design (Chupas *et al.*, 2008) with the addition of a U-shaped bracket for capillary support (Tsakoumis *et al.*, 2012). Additionally, our design offers the advantages of a compact size, with minimal ancillary equipment and its ability to be readily moved between beamlines, combined with a method to stabilize the capillary that minimizes its failure/shatter rate during installation, as noted above. When opting for resistive coil heating in the new design, it was practical to continue with the existing design of mounting the cell to the goniometer. However, given the variation in goniometer sizes at SSRL, and their ability to support different cantilevered weights, the new design also included a mounting option to a three-axis linear translational stage if needed.

The inlet and outlet to the cell consist of two 6061 aluminium alloy blocks with an assortment of holes for attaching the heaters, thermocouples and structural components, and for allowing the flow of gas to and from the cell as well as into and out of the capillary. The inlet and outlet sides of the cell have been expanded in size to accommodate linear bearings and alternative heaters on the outlet side of the cell, thus improving upon prior designs (Chupas *et al.*, 2008). Aluminium, used to fabricate the inlet and outlet blocks, was also chosen as a cost-effective way to reduce overall weight. The inlet and outlet blocks have a pair of holes below the capillary mounting location to accommodate two precision steel rods that join the two sides together. The holes to mount the steel rods on the outlet block (Fig. 2, section A–A) were machined to accommodate linear bearings in which the rods passed through. The addition of the bearings allows for the outlet block to slide freely over the length of the rods and aids in reducing the capillary failure rate when installing samples.

To mount the cell to the diffractometer in the hutch at the beamline, the outside face of the inlet block has a D-shaped aluminium peg welded into it so that it can be readily and securely attached to a goniometer head (Fig. S1). The D shape of the peg allows for alignment in the goniometer head and is advantageous if a 'rocking' scan is implemented. Due to the overall dimensions and weight of the cell, 20 cm long × 3.8 cm wide × 5.8 cm tall and approximately 600 g, an adapter plate was also fabricated allowing for mounting of the cell to a linear translation mounting stage through a Newport X48 rail system (see schematic in the supporting information) in the event a goniometer head could not support the cell.

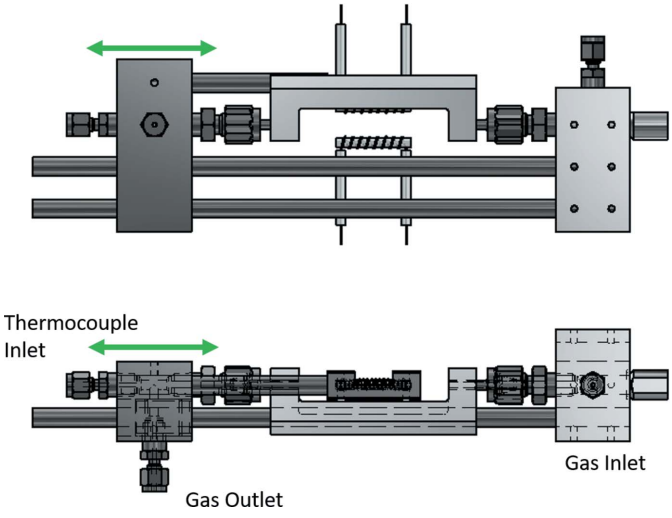

Figure 1
In situ capillary cell design for the characterization of powder samples in flowing atmospheres at elevated temperatures and pressures. (Top) Up-beam side of cell. (Bottom) Top-down showing flow path. The green arrow indicates movement of the outlet block to accommodate variable-length capillaries.

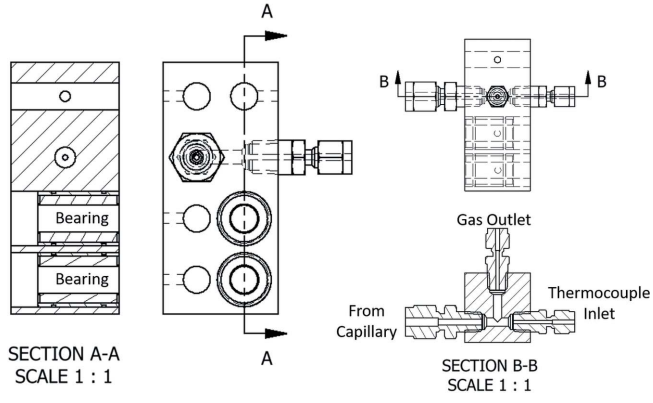

Figure 2
Outlet block of the capillary cell. Section A–A highlights the installation of linear bearings aiding in sample mounting. Section B–B highlights the internal 'T' consisting of the gas outlet (top), thermocouple inlet (right) and capillary inlet (left).

Compressed gas enters and exits the cell through 1/16-inch compression to 1/8-inch NPT fittings (Swagelok®). The choice of small diameter fittings and subsequent inlet and outlet 1/16-inch diameter tubing is to: (i) minimize the dead volume of the reactor resulting in faster purging of the gas atmosphere, especially at pressure; (ii) reduce the total volume of compressed gas or liquid in the lines in the event of catastrophic failure; and (iii) minimize the drag from the tubing and wires on the positioning motors on the goniometer head. Gas exits the cell through an identical 1/16-inch compression fitting on the up-beam side of the outlet block. The choice of the effluent stream exiting the cell up-beam rather than down-beam allows for a larger, unobstructed, solid angle to be scanned (Fig. 1). Having these compression fittings be removable instead of welded to the inlet and outlet blocks offers the ability to readily exchange the fittings to accommodate a variety of inlet tubing dimensions without the need for additional adapter fittings, which would increase the overall dead volume.

Compressed gas is fed to and from the capillary or U-frame through two 1/8-inch Swagelok compression fittings on the inlet and outlet blocks (Fig. 1). The 1/8-inch fittings allows for U-frame support capillaries up to 1.5 mm and compression fitting up to 3 mm with appropriate ferrules.

The outlet block acts as a 'T' fitting (Fig. 2, section B–B) where the capillary and gas outlet are perpendicular to one another, the thermocouple is mounted in a 1/16-inch compression fitting on the outside face of the outlet block, in line with the capillary. A graphite ferrule seals the thermocouple allowing for fine-tuning its placement inside the catalyst bed. Integrating the gas flow path into the support structure allows for smoother mounting of the capillary.

The outlet block also contains a pair of holes directly above and below the capillary mounts to secure the support rods for the resistive heaters. The distance between the center of the capillary and the center of the heater support rod mounting holes is 14.2 cm. The increase in distance [from 9.5 mm in the Chupas design (Chupas *et al.*, 2008) to 14.2 mm] between the sample and the heater mounts offers two benefits. First, the heaters can be moved farther away from the center of the sample allowing for larger-diameter capillaries to be used. Second, the coiled heating element can be placed farther away from the stainless steel support rod, minimizing heat transfer from the hot element to the cell itself improving thermal efficiency and safety.

The heater assembly consists of a stainless steel rod that supports a ceramic/resistive wire heating element (Fig. S2). Kanthal A-1 wire (22 gauge), selected for its high-temperature limit, 1623 K, is wrapped around alumina rods (Omega, Omegatite 450), with two additional alumina rods, forming a U-shape, acting as an electrical insulation between the Kanthal and the heater support rods. Approximately 30 cm of Kanthal wire is used in each heating element giving about 50 W of power at 24 V DC. Two heater assemblies are mounted one above and one below the capillary, and wired in series to deliver 100 W of power at 24 V DC.

Catalyst samples, either meshed particles or powder, are packed into the center of an appropriate capillary and immobilized between two plugs of quartz wool. When mounted in the cell the thermocouple is used as a back-stop to prevent the sample from potentially being blown out of the cell under high gas flow. The capillary is mounted into the cell using two different methods depending on the capillary diameter or materials of construction. For capillaries with an outer diameter (OD) between 1.5 and 3 mm, the capillary is directly mounted between the inlet and outlet blocks of the cell. The seal between the capillary and the cell is formed using graphite or Vespel ferrules. This mounting method has been successfully demonstrated using thick-walled (>0.1 mm wall thickness) Kapton and glass/quartz capillaries. However, thin-walled (*e.g.* 0.01 mm thickness) Kapton and glass tubes run the risk of collapsing during the compression step. This could readily be alleviated by an insert to firm up the end of the capillary, or potentially through the use of Viton or other elastomer O-rings to complete the seal.

For capillary tubes with an OD of less than 1.5 mm, a U-frame support (Fig. 3) is used. Once loaded with the sample, the capillary is positioned inside the U-frame and epoxied in place using a two-part epoxy, such as JB Weld. Curing times and temperatures vary between epoxy types and brands with all cure times taking longer than using O-rings to form the seal, requiring an additional degree of planning for sample preparation and experimentation. Once cured, the port connectors on the U-frame are attached to the inlet and outlet blocks. The adaptation of the U-frame as an alternate means to attach capillaries to the cell minimizes the stress, and breakage, on the smaller-diameter or thinner-walled capillaries.

The last component of the cell is a safety/thermal shield (Fig. S3). The shield is fabricated from a 3D-printed nylon frame that supports two 0.005-inch thick polyimide windows. The two halves of the shield are magnetically clamped to each other and wrap around the cell. The inlet side of the shield contains a large-area Kapton window perpendicular to the beam path allowing for a large sample positioning area. The detector side of the shield is curved allowing for $2\theta = \pm 60^{\circ}$ offering a large angle for scattering measurements. This shield protects both the operator and beamline equipment in the unlikely case of catastrophic failure of the capillary. The shield also minimizes drafts in the local area increasing the thermal stability of the system.

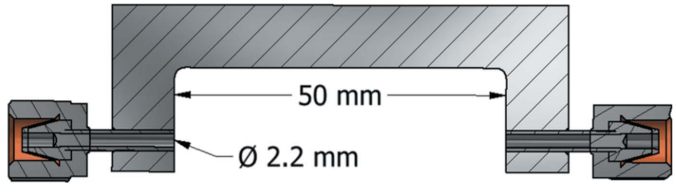

Figure 3
U-shaped support for capillaries less than 1.5 mm in diameter.

4. Performance characteristics

A 1.5 mm OD × 1.0 mm inner diameter (ID) borosilicate capillary (Kimble, No. 2502) was filled with a 5 mm-long bed of MCM-41 silica (Sigma Aldrich), supported by quartz wool on both ends. The capillary was mounted in the U-frame using two-part epoxy (JB Weld) and, after the epoxy cured, approximately 24 h, the U-frame was mounted between the inlet and outlet blocks. The cell was tested using a variety of temperature ramps, and it was determined that minimum and maximum controllable ramps were 2 and 50 K min^{-1}, respectively. With power limited to 100 W (24 V DC, 4 A) to the heating elements, the cell was readily able to reach the thermal limit of the borosilicate capillary, 870 K. However, using a 1.0 mm OD × 0.98 mm ID quartz capillary (Charles Supper), and the addition of a reflector (Fig. S4), 200 W of power (32 V, 6.25 A) was able to heat a quartz capillary to 1373 K at a controlled temperature ramp of 100 K min^{-1}. A maximum temperature of 1437 K was achieved and sustained for 10 min before the heating element failed. These tests demonstrated that a broad range of temperatures and thermal ramp rates can be used in the cell and would work for *in situ* XRD measurements during catalyst testing.

At room temperature, the borosilicate capillary was pressurized to 34 bar without failure, demonstrating the potential for *in situ* high-pressure experimentation. The 0.98 mm OD × 1 mm ID quartz capillary was epoxied into the U-frame and also pressure tested. After 18 bar of pressure the quartz capillary failed. This is a lower working pressure than has been reported by others (Jensen *et al.*, 2010). We note, however, that for this test we used a sealed quartz capillary with a funnel end, requiring that both ends of the capillary had to be broken for appropriate mounting and it is likely that this creates defects or micro-fractures in the quartz leading to the failure at lower pressures. This could be mitigated using more expensive open-ended capillaries. Given pressure requirements of 20 bar, the borosilicate capillary was selected for catalyst testing.

The XRD cell was mounted on the linear translation stage at beamline 2-1 at the Stanford Synchrotron Radiation Lightsource (SSRL) and 2θ was scanned using a monochromatic 15.50 keV beam to characterize the scattering performance of the 1.5 mm OD × 1.0 mm ID borosilicate capillary. Diffraction patterns were collected using a Pilatus 100K two-dimensional area detector. The background scattering by the empty borosilicate capillary, mounted in the cell with the safety shield installed, is presented in Figs. S5 and S6. The maximum detector angle above the incident beam where scattering data can be acquired is 55° (Fig. S5). At larger angles the safety/thermal enclosure and cell block the beam. As borosilicate glass is an amorphous material, the background scattering does not contain any sharp diffraction peaks making it advantageous for the catalyst characterization since there are no diffraction features that could interfere with or cover weak diffraction peaks from the sample (Fig. S6). Comparing the direct X-ray beam intensity with the intensity after passing through the cell, 44% of the incident photons are transmitted. Most of this loss can be attributed to absorption by the glass tube which we calculated to transmit 63% of 15.50 keV X-rays.

5. Demonstration of cell performance using cobalt-based F–T catalysts

Cobalt supported on silica has been a much-studied catalyst for the F–T synthesis of hydrocarbons from syngas (H_2 + CO) (Jung *et al.*, 2012; Ohtsuka *et al.*, 2003; Saib *et al.*, 2002; Wolf *et al.*, 2017). The F–T synthesis offers a variety of process conditions, temperatures and pressures during its activation and reaction steps to demonstrate the versatility of the capillary cell. The Co/SiO_2 catalyst was synthesized by wet impregnation of the silica support and then calcined to form cobalt particles (Singh *et al.*, 2018). During the F–T synthesis, the catalyst was first activated by reduction at 723 K in flowing H_2 at atmospheric pressure for 30 min and was then tested for F–T synthesis at 523 K at 20 bar in a flow of 2:1 H_2:CO for 3 h. To form the carbide, the H_2 flow was stopped and the temperature and pressure of 100% CO were maintained at 523 K and 20 bar for 7 h.

5.1. *In situ* XRD characterizing the reduction of a Co/SiO_2 catalyst

The Co/SiO_2 catalyst, in powder form, was loaded into a 1.5 mm OD × 1.0 mm ID borosilicate capillary and the capillary was epoxied into the U-frame. The capillary and U-frame assembly were mounted into the inlet and outlet blocks of the cell as discussed above. A flow rate of 20 ml min^{-1} hydrogen was established at atmospheric pressure; the temperature of the cell was ramped from 298 to 723 K at a rate of 10 K min^{-1} and held at 723 K for 30 min. During the temperature ramp, the wide-angle X-ray scattering over a q-range from 2.5 to 3.6 $Å^{-1}$ was recorded with a Pilatus 100K two-dimensional area detector. During acquisition, five images were acquired by moving the 2θ angle of the detector to span the entire range. The images were stitched together in the data processing software to form a diffraction pattern which took approximately 2 min to acquire. The temperature assigned to each diffraction pattern was defined as the temperature of the first image in each scan, with one complete diffraction pattern consisting of five images, corresponding to approximately a 19 K change in sample temperature.

The resulting diffraction data as a function of temperature during the reduction are presented in Fig. 4(*a*). Selected diffraction patterns at specific temperatures are presented in Fig. 4(*b*). The data suggest that there are three distinct crystalline phases during the reduction process as the temperature is increased from 298 to 723 K. The SiO_2 support was determined to be amorphous, such that all diffraction peaks could be ascribed to reflections of cobalt or cobalt oxide phases.

The diffraction pattern characterizing the initial state of the Co/SiO_2 catalyst (Fig. 4*b*) contains peaks at 2.59, 2.70 and 3.12 $Å^{-1}$ corresponding to lattice spacings of 2.427, 2.325 and 2.015 Å, respectively. These d-spacings match the (311), (222)

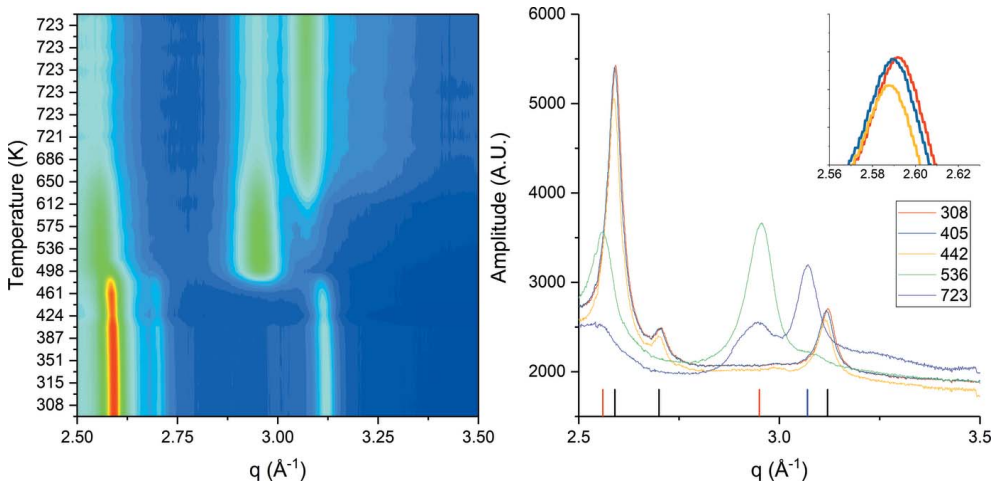

Figure 4
Diffraction patterns collected during the temperature-programmed reduction from 298 to 723 K of the Co/silica gel catalyst in flowing H_2 (left), and select diffraction patterns as a function of temperature during the reduction (right) with reference patterns of Co_3O_4 (black), CoO (red) and f.c.c. Co (blue) displayed below. Inset: close-up of the top of the diffraction peak near 2.59 Å^{-1} highlighting the shift in peak position as a function of temperature.

and (400) reflections of Co_3O_4 (PDF card 00-042-1467) identifying the initial state of the Co in the fresh, calcined catalyst as Co_3O_4. Using analysis of the (311) Co_3O_4 reflection with the Scherer equation results in an average diameter of the Co_3O_4 particles of 14 nm, in good agreement with transmission electron microscopy images (Singh *et al.*, 2018).

As the temperature increased from 405 to 442 K, there is a shift in the diffraction peak positions (Fig. 4) to lower q values corresponding to lattice expansion. An example of this is the peak starting at 2.59 Å^{-1} and shifting to 2.58 Å^{-1} as temperature increased from 308 to 442 K (Fig. 4*b*, inset), which represents an expansion of the (311) reflection from 2.427 to 2.429 Å, matching work previously reported (Broemme, 1991). Since this observation matches the literature, we conclude that the cell was functioning properly as an *in situ* powder XRD experimental cell.

As the temperature further increased from 442 to 536 K, the overall intensity of the diffraction peaks associated with the Co_3O_4 phase decrease in intensity with a continued increase in expansion of the lattice (Fig. 4). Between 476 and 536 K there is a rapid change in the diffraction pattern with the disappearance of all peaks associated with Co_3O_4 and the formation of two new peaks at 2.56 and 2.95 Å^{-1} (Fig. 4*a*). These peaks correspond to d-spacings of 2.454 and 2.128 Å matching the (111) and (200) reflections of CoO (PDF card 00-048-1719) and indicating the reduction of the Co(II)/Co(III) oxide (Co_3O_4) phase to Co(II) oxide (CoO). The complete transition of Co_3O_4 to CoO occurred by 548 K. The reduction of $Co^{2+/3+}$ to Co^{2+} between 510 and 529 K matches prior *in situ* XRD studies with the phase change occurring between 473 and 573 K (Smith *et al.*, 2012), 523 and 623 K (Ducreux *et al.*, 2009) and around 573 K (Cats & Weckhuysen, 2016). This relatively large range in the reported reduction temperature of Co_3O_4 to CoO is likely dependent upon differences in the ramp rate used during the reduction, the crystallite site of the oxide NPs, the wt% loading, and other factors.

A new peak at q = 3.07 Å^{-1} starts to form as the reduction temperature reaches 573 K (Fig. 4*a*). This correspond to a lattice spacing of 2.038 Å, assigned to f.c.c. Co (PDF card 00-015-0806). As the temperature increases from 573 to 723 K the peaks at 2.55 and 2.96 Å^{-1} decrease in intensity while the peak at 3.07 Å^{-1} increases, indicating a conversion from CoO to f.c.c. Co. Even after an isothermal hold in flowing H_2 at 723 K, there is incomplete conversion from CoO to metallic Co phase (Fig. 4*b*) as evident by the diffraction peak at 2.95 Å^{-1}. These results are comparable with previous *in situ* XRD studies where the reduction of CoO to Co^0 has been observed from 523 to 673 K (Smith *et al.*, 2012; Eschemann *et al.*, 2016).

5.2. *In situ* XRD characterizing the Co/SiO_2 catalyst under reaction conditions

After the catalyst activation (reduction at 723 K for 30 min), the sample cell temperature was reduced to 523 K. The cell quickly stabilized at the new set-point temperature (<10 min) without supplemental cooling due to its low thermal mass. The hydrogen flow was replaced for a 2:1 H_2:CO flow and the pressure was slowly increased to 20 bar over 30 min. There were no observable changes to the *in situ* diffraction pattern throughout the 3 h time on stream under these F–T reaction conditions. This is in agreement with prior work under these reaction conditions for a cobalt-based catalyst (Cats & Weckhuysen, 2016; Karaca *et al.*, 2011).

5.3. *In situ* XRD characterizing the carburization of the Co/SiO_2 catalyst

After the reaction step, the gas flow was switched to a pure CO feed (80 ml min^{-1}) maintaining temperature and pressure of 523 K and 20 bar, with the aim of converting the metallic Co NPs to Co_2C. The q-range of each scan was extended from 2.5–3.6 Å^{-1} to 2.5–6.2 Å^{-1}. Prior work has shown that it is possible to carburize Co to Co_2C using a pure CO atmosphere at 1 bar

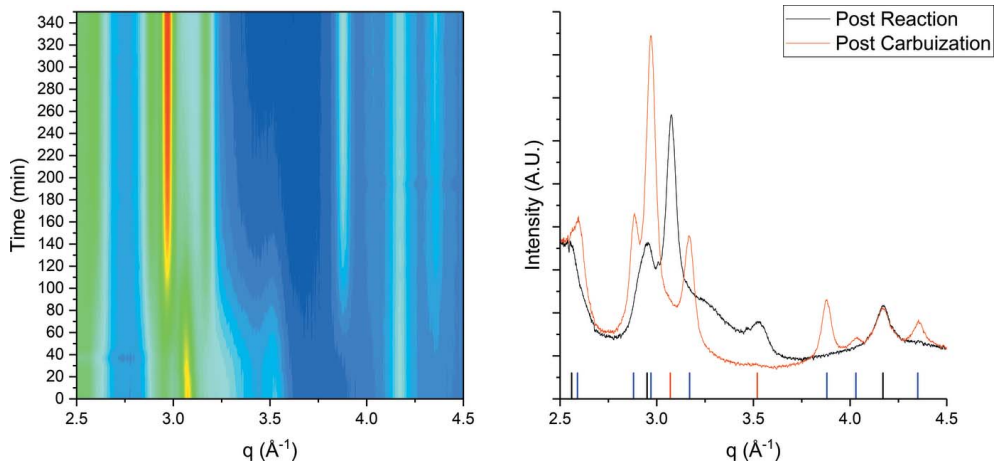

Figure 5
Diffraction patterns collected during the carburization of the reduced Co/silica gel catalyst in 20 bar CO at 523 K as a function of time since hydrogen was removed from the gas stream (left) and diffraction patterns at 0 and 340 min, prior to and post carburization (right) with reference patterns of CoO (black), f.c.c. Co (red) and Co_2C (blue) displayed below.

pressure (Ducreux *et al.*, 2009; Kwak *et al.*, 2013; Pei *et al.*, 2015). However, these studies showed that the carbide phase formed very slowly at 1 bar CO and it took tens of hours of reaction to fully carburize the cobalt to Co_2C.

Fig. 5 shows the results of *in situ* XRD during the carburization as a function of time from when the hydrogen flow was stopped. The initial diffraction pattern includes peaks at 2.95, 3.07, 3.52 and 4.17 Å^{-1} previously identified as f.c.c. Co and CoO. As time progresses, and the H_2 is purged from the system, the diffraction peaks corresponding to f.c.c. Co, at 3.07 and 3.52 Å^{-1}, decrease in intensity and broaden over 200 min while new peaks at 2.59, 2.88, 2.97, 3.17, 3.88, 4.03 and 4.35 Å^{-1} form. The onset of change starts to occur at around 40 min, matching the similar time constant of the experimental setup (25 min). The peaks associated with CoO have no appreciable change during the carburization process. The intensity of the new diffraction peaks stabilized after ~300 min and correspond to the *d*-spacings of 2.180, 2.115 and 1.984 Å and are identified as (002), (111) and (021) reflections of Co_2C (PDF card 04-004-4639).

With the ability to conduct the carburization at high pressure (20 bar CO) we observed near complete carburization of the Co in only 4 h. This is substantially faster than the previously noted *in situ* XRD study at atmospheric pressure that showed that even after 15 h there was still significant metallic f.c.c. Co present (Ducreux *et al.*, 2009). Hence the higher-pressure capabilities of the current cell enables more rapid processes such as phase changes to be achieved.

6. Conclusions

An *in situ* capillary XRD cell for studying powder samples under gas flow at elevated temperatures was designed, fabricated and tested at SSRL. The main body of the cell shows that it is a viable flow cell and the materials of construction of the capillary that holds the sample will dictate the temperature and pressure operating limits. A test case characterizing the state of Co in a Co/SiO_2 catalyst for Fischer–Tropsch synthesis demonstrated the cell's performance as well as the temporal resolution of beamline 2-1. The study showed that Co_3O_4 reduces to f.c.c. Co through a short-lived intermediate CoO phase, and that the f.c.c. Co readily reacts to form Co_2C in the presence of high-pressure CO (20 bar, 523 K) while residual CoO does not carburize. The development of this cell offers new capabilities for *in situ* XRD studies of catalysts at the scattering beamlines at SSRL.

APPENDIX *A*
Experimental methods

A1. Catalyst synthesis

Co/silica catalysts were prepared through the incipient wetness impregnation of silica gel (Davisil 643) with $Co(NO_3)_2{\cdot}6H_2O$ (Aldrich) dissolved in deionized water to give a Co loading of 10 wt%. After impregnation, samples were dried at room temperature and calcined at 623 K in air for 4 h.

A2. XRD measurements

X-ray diffraction was performed at beamline 2-1 at SSRL using a 15.50 keV incident photon energy and a Pilatus 100K two-dimensional detector. Sample position was controlled using a three-axis linear motorized stage. The incident angle was fixed and the 2θ angle controlled by moving the two-dimensional detector. LaB_6 was used as a calibration standard.

A3. *In situ* powder XRD of Co/SiO_2 under reduction and carburization conditions

Samples were pelletized, crushed and then sieved to remove fines that could clog the capillary. A small plug of glass wool was first put in the capillary, followed by the catalyst powder, and then another plug of glass wool to hold the catalyst in place. The glass capillary was glued into the frame using

JB Weld epoxy and allowed to cure overnight. When attaching the frame to the reactor, the thermocouple was positioned such that the tip contacted the quartz wool plug on the inlet side of the capillary.

Catalysts were reduced in flowing H_2 metered using a mass flow controller (MFC; Brooks). H_2, 20 ml min^{-1}, was flowed through the catalysts bed while the catalyst was heated to 723 K at 10 K min^{-1}. During the reduction, images were collected using the two-dimensional detector. Images were collected from 21° to 25° 2θ using a 1° 2θ step size and a 20 s integration time.

The catalysts were carburized at 523 K using flowing CO. CO was purified by passing through a Matheson Nanochem Metal-X purifier. CO, 80 ml min^{-1}, was metered using a MFC. The catalyst was held at 20 bar pressure using a back pressure regulator (Swagelok) and the pressure measured using an electronic pressure transducer (Setra).

A4. XRD data processing

Each 2θ scan resulted in a two-dimensional image taken at each angle. Each image was processed to convert from the two-dimensional positions to a one-dimensional intensity *versus* 2θ measurement. The resulting series of one-dimensional 2θ scans for each angle were stitched together to have a one-dimensional intensity *versus* 2θ measurement for the entire scan range.

For the carburization and reduction experiments, a silica gel reference was recorded using the same scan range, scan step and integration time to measure the background signal of the support and capillary. The diffraction pattern characterizing the silica gel and capillary was subtracted from the sample diffraction patterns for background removal.

Acknowledgements

Use of the Stanford Synchrotron Radiation Lightsource, SLAC National Accelerator Laboratory, is supported by the US Department of Energy, Office of Science, Office of Basic Energy Sciences under Contract No. DE-AC02-76SF00515 (JAS). The authors would like to thank Charles Troxel for his help in implementing the cell at beamline 2-1 at SSRL. The authors would also like to thank Doug Van Campen, Magnus Rønning and Apurva Mehta for discussions regarding design considerations.

Funding information

The following funding is acknowledged: US Department of Energy, Office of Science, Office of Basic Energy Sciences (contract No. DE-AC02-76SF00515); US Department of Energy Office of Basic Energy Sciences to the SUNCAT Center for Interface Science and Catalysis.; National Science Foundation Graduate Research Fellowship (grant No. DGE-114747).

References

Ail, S. S. & Dasappa, S. (2016). *Renewable Sustainable Energy Rev.* **58**, 267–286.
Bansode, A., Guilera, G., Cuartero, V., Simonelli, L., Avila, M. & Urakawa, A. (2014). *Rev. Sci. Instrum.* **85**, 084105.
Broemme, A. D. D. (1991). *IEEE Trans. Electr. Insul.* **26**, 4.
Cats, K. H., Andrews, J. C., Stéphan, O., March, K., Karunakaran, C., Meirer, F., de Groot, F. M. F. & Weckhuysen, B. M. (2016). *Catal. Sci. Technol.* **6**, 4438–4449.
Cats, K. H., Gonzalez-Jimenez, I. D., Liu, Y., Nelson, J., van Campen, D., Meirer, F., van der Eerden, A. M. J., de Groot, F. M. F., Andrews, J. C. & Weckhuysen, B. M. (2013). *Chem. Commun.* **49**, 4622–4624.
Cats, K. H. & Weckhuysen, B. M. (2016). *ChemCatChem*, **8**, 1531–1542.
Chupas, P. J., Chapman, K. W., Kurtz, C., Hanson, J. C., Lee, P. L. & Grey, C. P. (2008). *J. Appl. Cryst.* **41**, 822–824.
Chupas, P. J., Ciraolo, M. F., Hanson, J. C. & Grey, C. P. (2001). *J. Am. Chem. Soc.* **123**, 1694–1702.
Clausen, B. S., Gråbaek, L., Steffensen, G., Hansen, P. L. & Topsøe, H. (1993). *Catal. Lett.* **20**, 23–36.
Clausen, B. S., Steffensen, G., Fabius, B., Villadsen, J., Feidenhans'l, R. & Topsøe, H. (1991). *J. Catal.* **132**, 524–535.
Ducreux, O., Rebours, B., Lynch, J., Roy-Auberger, M. & Bazin, D. (2009). *Oil Gas Sci. Technol. Rev. IFP*, **64**, 49–62.
Eschemann, T. O., Oenema, J. & de Jong, K. P. (2016). *Catal. Today*, **261**, 60–66.
Jensen, T. R., Nielsen, T. K., Filinchuk, Y., Jørgensen, J.-E., Cerenius, Y., Gray, E. M. & Webb, C. J. (2010). *J. Appl. Cryst.* **43**, 1456–1463.
Jung, J.-S., Kim, S. W. & Moon, D. J. (2012). *Catal. Today*, **185**, 168–174.
Karaca, H., Safonova, O. V., Chambrey, S., Fongarland, P., Roussel, P., Griboval-Constant, A., Lacroix, M. & Khodakov, A. Y. (2011). *J. Catal.* **277**, 14–26.
Khodakov, A. Y., Chu, W. & Fongarland, P. (2007). *Chem. Rev.* **107**, 1692–1744.
Kwak, G., Woo, M. H., Kang, S. C., Park, H.-G., Lee, Y.-J., Jun, K.-W. & Ha, K.-S. (2013). *J. Catal.* **307**, 27–36.
Lebarbier, V. M., Mei, D., Kim, D. H., Andersen, A., Male, J. L., Holladay, J. E., Rousseau, R. & Wang, Y. (2011). *J. Phys. Chem. C*, **115**, 17440–17451.
Meunier, F. C. (2010). *Chem. Soc. Rev.* **39**, 4602–4614.
O'Brien, M. G., Beale, A. M., Jacques, S. D. M. & Weckhuysen, B. M. (2009). *Top. Catal.* **52**, 1400–1409.
Ohtsuka, Y., Arai, T., Takasaki, S. & Tsubouchi, N. (2003). *Energy Fuels*, **17**, 804–809.
Pei, Y.-P., Liu, J.-X., Zhao, Y.-H., Ding, Y.-J., Liu, T., Dong, W.-D., Zhu, H.-J., Su, H.-Y., Yan, L., Li, J.-L. & Li, W.-X. (2015). *ACS Catal.* **5**, 3620–3624.
Price, S. W. T., Martin, D. J., Parsons, A. D., Sławiński, W. A., Vamvakeros, A., Keylock, S. J., Beale, A. M. & Mosselmans, J. F. W. (2017). *Sci. Adv.* **3**, e1602838.
Rønning, M., Tsakoumis, N. E., Voronov, A., Johnsen, R. E., Norby, P., van Beek, W., Borg, Ø., Rytter, E. & Holmen, A. (2010). *Catal. Today*, **155**, 289–295.
Saib, A. M., Claeys, M. & van Steen, E. (2002). *Catal. Today*, **71**, 395–402.
Singh, J. A., Schumann, J., Hoffman, A. S., Boubnov, A., Asundi, A. S., Nørskov, J. K., Bare, S. R. & Bent, S. F. (2018). *ChemCatChem.* Submitted.
Smit, E. de, Beale, A. M., Nikitenko, S. & Weckhuysen, B. M. (2009). *J. Catal.* **262**, 244–256.
Smit, E. de, Cinquini, F., Beale, A. M., Safonova, O. V., van Beek, W., Sautet, P. & Weckhuysen, B. M. (2010). *J. Am. Chem. Soc.* **132**, 14928–14941.
Smith, M. L., Campos, A. & Spivey, J. J. (2012). *Catal. Today*, **182**, 60–66.
Staniuk, M., Hirsch, O., Kränzlin, N., Böhlen, R., van Beek, W., Abdala, P. M. & Koziej, D. (2014). *Chem. Mater.* **26**, 2086–2094.

Su, J., Zhang, Z., Fu, D., Liu, D., Xu, X.-C., Shi, B., Wang, X., Rui, S., Jiang, Z., Xu, J. & Han, Y.-F. (2016). *J. Catal.* **336**, 94–106.
Tsakoumis, N. E., Dehghan, R., Johnsen, R. E., Voronov, A., van Beek, W., Walmsley, J. C., Borg, Ø., Rytter, E., Chen, D., Rønning, M. & Holmen, A. (2013). *Catal. Today*, **205**, 86–93.
Tsakoumis, N. E., Rønning, M., Borg, Ø., Rytter, E. & Holmen, A. (2010). *Catal. Today*, **154**, 162–182.
Tsakoumis, N. E., Voronov, A., Rønning, M., van Beek, W., Borg, Ø., Rytter, E. & Holmen, A. (2012). *J. Catal.* **291**, 138–148.
Wolf, M., Kotzé, H., Fischer, N. & Claeys, M. (2017). *Faraday Discuss.* **197**, 243–268.